



## Interaction between L-aspartate and the brucite [Mg(OH)<sub>2</sub>]-water interface

Charlene F. Estrada<sup>a,b,\*</sup>, Dimitri A. Sverjensky<sup>a</sup>, Manuel Pelletier<sup>c,d</sup>,  
Angéline Razafitianamaharavo<sup>c,d</sup>, Robert M. Hazen<sup>b</sup>

<sup>a</sup> Johns Hopkins University, Dept. of Earth & Planetary Sciences, 3400 N Charles St, Baltimore, MD 21218, USA

<sup>b</sup> Geophysical Laboratory, Carnegie Institution of Washington, Broad Branch Rd NW, Washington, DC 20015, USA

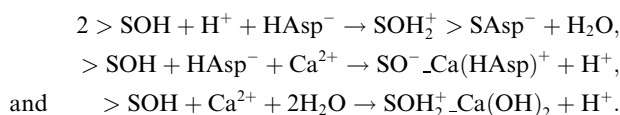
<sup>c</sup> Université de Lorraine, Laboratoire Interdisciplinaire des Environnements Continentaux, 15 avenue du Charmois,  
54500 Vandœuvre les Nancy, France

<sup>d</sup> CNRS, UMR 7360, Laboratoire Interdisciplinaire des Environnements Continentaux, 15 avenue du Charmois,  
54500 Vandœuvre les Nancy, France

Received 17 May 2014; accepted in revised form 1 February 2015; available online 11 February 2015

### Abstract

The interaction of biomolecules at the mineral–water interface could have played a prominent role in the emergence of more complex organic species in life's origins. Serpentine-hosted hydrothermal vents may have acted as a suitable environment for this process to occur, although little is known about biomolecule–mineral interactions in this system. We used batch adsorption experiments and surface complexation modeling to study the interaction of L-aspartate onto a thermodynamically stable product of serpentinization, brucite [Mg(OH)<sub>2</sub>], over a wide range of initial aspartate concentrations at four ionic strengths governed by [Mg<sup>2+</sup>] and [Ca<sup>2+</sup>]. We observed that up to 1.0 μmol of aspartate adsorbed per m<sup>2</sup> of brucite at pH ~ 10.2 and low Mg<sup>2+</sup> concentrations (0.7 × 10<sup>-3</sup> M), but surface adsorption decreased at high Mg<sup>2+</sup> concentrations (5.8 × 10<sup>-3</sup> M). At high Ca<sup>2+</sup> concentrations (4.0 × 10<sup>-3</sup> M), aspartate surface adsorption doubled (to 2.0 μmol m<sup>-2</sup>), with Ca<sup>2+</sup> adsorption at 29.6 μmol m<sup>-2</sup>. We used the extended triple-layer model (ETLM) to construct a quantitative thermodynamic model of the adsorption data. We proposed three surface reactions involving the adsorption of aspartate (HAsp<sup>-</sup>) and/or Ca<sup>2+</sup> onto brucite:



We used the ETLM to predict that brucite particle surface charge becomes more negative with increasing [Mg<sup>2+</sup>], creating an unfavorable electrostatic environment for a negatively-charged aspartate molecule to adsorb. In contrast, our addition of Ca<sup>2+</sup> to the system resulted in Ca<sup>2+</sup> adsorption and development of positive surface charge. Our prediction of surface speciation of aspartate on brucite with Ca<sup>2+</sup> revealed that the calcium–aspartate complex is the predominant surface aspartate species, which suggests that the increase in aspartate adsorption with Ca<sup>2+</sup> is primarily driven by calcium adsorption. The cooperative effect of Ca<sup>2+</sup> and the inhibitive effect of Mg<sup>2+</sup> on aspartate adsorption onto brucite indicate that serpentine-hosted hydrothermal fluids provide an ideal environment for these interactions to take place.

© 2015 Elsevier Ltd. All rights reserved.

\* Corresponding author at: Geophysical Laboratory, Carnegie Institution of Washington, 5251 Broad Branch Rd NW, Washington, DC 20015, USA. Tel.: +1 202 478 8900.

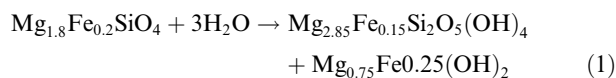
E-mail address: [cestrada@jhu.edu](mailto:cestrada@jhu.edu) (C.F. Estrada).

## 1. INTRODUCTION

The origin of life on early Earth was a geochemical sequence of emergent steps involving increasing complexity (Hazen, 2005). Among the first of these steps was the synthesis of prebiotic organic molecules in the midst of the Archean atmosphere, ocean, and lithologies. The emergence of simple molecules such as amino acids and sugars may have occurred under a variety of plausible Archean environments (Ponnamperuma and Pering, 1966; Deamer and Pashley, 1989; Hennet et al., 1992; Holm and Andersson, 2005; Jalbout et al., 2007; Cleaves et al., 2008; Kim et al., 2011). Far less is known about the selection, concentration, and self-organization of these biomolecules into macromolecular systems from dilute solutions.

Mineral surfaces may provide the means by which simple biomolecules self-organize. The mineral–water interface is known to concentrate biomolecules through adsorption (Jonsson et al., 2009, 2010; Cleaves et al., 2012). Mineral surfaces change significantly with shifts in pH owing to surface protonation reactions. Accordingly, mineral surfaces may have potentially played a key role in the origin of life, whereby the mineral–water interface provided sites for the selection, concentration, and self-organization of biomolecules (Goldschmidt, 1952; Hazen, 2006; Cleaves et al., 2012).

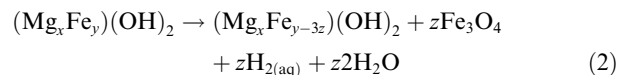
Hydrothermal vent systems have been discussed as plausible environments for the origin of life by providing templates for macromolecular assembly (Baross and Hoffman, 1985; Shock and Canovas, 2010; Sleep et al., 2011). The disequilibria established by mixing hot, hydrothermal fluids (<350 °C) with the overlying cold seawater (2 °C) may drive the formation of some prebiotic molecules (Shock and Schulte, 1998; Shock and Canovas, 2010). A different type of hydrothermal system known as the Lost City hydrothermal field was discovered off the Mid-Ocean Ridge Axis (Kelley et al., 2001). The Lost City hydrothermal field belongs to a class of hydrothermal systems that undergo serpentinization, which involves the hydration of magnesium-rich olivine to serpentine and ferro-brucite (Bach et al., 2006), according to the reaction:



Serpentinite-hosted hydrothermal vents such as the Lost City hydrothermal field release fluids that contain up to  $19 \times 10^{-3}$  M and  $4 \times 10^{-3}$  M of  $\text{H}_2$  and  $\text{CH}_4$ , respectively (Kelley et al., 2005; Proskurowski et al., 2006). The mixing of these hydrothermal fluids with seawater creates a strong redox gradient that may facilitate the formation of prebiotic molecules (Holm et al., 2006; Shock and Canovas, 2010). Furthermore, greenstone sequences discovered at the Isua Formation (3.8 Ga) and the Pilbara Formation (3.5 Ga) suggest that serpentinite-hosted hydrothermal activity may have been present on early Earth (Dymek et al., 1988; Van Kranendonk et al., 2007; Shibuya et al., 2010). These localities and the presence of Archean komatiites provide evidence that the oceanic crust on early Earth was more ultramafic

compared to today's mafic, basalt-hosted seafloor (Herzberg et al., 2010; Van Kranendonk, 2010). Depending on the prevalence of the ultramafic host rock, serpentinite-hosted hydrothermal fields may have been prolific on the Archean seafloor prior to the emergence of the first cellular lifeform at 3.48 Ga (Noffke et al., 2013).

Ferro-brucite [ $\text{Mg}_{0.75}\text{Fe}_{0.25}(\text{OH})_2$ ] is a thermodynamically stable mineral of the serpentinization reaction in Eq. (1). The ferrous iron in ferro-brucite controls the amount of  $\text{H}_{2(\text{aq})}$  produced in the hydrothermal field as magnetite is subsequently precipitated:



As this reaction proceeds to the right, the amount of  $\text{H}_{2(\text{aq})}$  flowing through the system becomes limited, and the brucite in the serpentinite-hosted hydrothermal field approaches the magnesium endmember (Bach et al., 2006; McCollom and Bach, 2009). Holm et al. (2006) and Holm (2012) have suggested that magnesium plays a role in stabilizing prebiotic biomolecules such as proteins and nucleic acids. As the primary constituent of brucite, magnesium may promote the formation of more complex molecules at the mineral–water interface within a serpentinite-hosted hydrothermal system.

Previous studies of brucite surface chemistry have focused on its precipitation and dissolution kinetics (Hostetler, 1963; Schott, 1981; Jordan and Rammensee, 1996; Pokrovsky and Schott, 2004; Pokrovsky et al., 2005; Kudoh et al., 2006). Nevertheless, few studies exist on the adsorption of organic species onto the brucite surface over a wide range of conditions. Pokrovsky and coworkers (2005) have studied the effect of oxalate, citrate, glycine, xylose, and catechol on brucite dissolution and precipitation. These biomolecules affected brucite dissolution at concentrations greater than  $1 \times 10^{-2}$  M and at neutral to weakly alkaline pH conditions. Citrate adsorbed in amounts as high as  $0.4 \mu\text{mol m}^{-2}$ , and it and the other biomolecules may have attached onto the brucite surface as an inner-sphere species (Pokrovsky et al., 2005). The authors also observed that concentrations of at least  $1 \times 10^{-2}$  M  $\text{Ca}^{2+}$  increase the brucite dissolution rate at pH = 4.9, and they assumed that calcium might adsorb onto brucite as a bidentate or monodentate mononuclear surface species.

In this investigation, we characterized the adsorption of the amino acid L-aspartate ( $\text{C}_4\text{H}_7\text{NO}_4$ ) onto powdered brucite. Aspartate is a polar amino acid with three protonation sites: two carboxyl groups and one amine group. Hennet and coworkers (1992) synthesized aspartate under mineral-buffered, simulated hydrothermal conditions. The adsorption of aspartate has been previously well-characterized on rutile (Giacomelli et al., 1995; Roddick-Lanzilotta and McQuillan, 2000; Jonsson et al., 2010), calcite (Hazen et al., 2001), kaolinite (Ikhsan et al., 2004), and alumina (Greiner et al., 2014). However, there are no studies on the adsorption of aspartate on brucite under the effect of variable divalent cation concentration, molecular concentration, and/or pH conditions.

The aim of this study is to evaluate the potential role that minerals within serpentinite-hosted hydrothermal fields play in concentrating and selecting prebiotic molecules from a dilute aqueous environment. In this framework, we characterized the extent and possible importance of this interaction with a combination of batch adsorption experiments at 25 °C and 1 bar and surface complexation modeling. Furthermore, we investigated the effects that common dissolved ions, including  $\text{Mg}^{2+}$  and  $\text{Ca}^{2+}$ , have on the interaction between aspartate and the brucite–water interface so that we may predict mineral surface reactions in plausible prebiotic aqueous environments.

## 2. MATERIALS AND METHODS

### 2.1. Brucite synthesis

We synthesized a microcrystalline brucite powder with a precipitation method previously reported by Henrist and coworkers (2003) and Lu and coworkers (2004). With 18.2 M $\Omega$ -cm Milli-Q water (Millipore), we prepared a 2.0 M  $\text{MgCl}_2$  solution (99.99% Alfa Aesar dry ampoules under Ar gas) and a solution containing 2.0 M  $\text{NH}_4\text{OH}$  (Sigma–Aldrich, 25 wt.% solution). We added the  $\text{MgCl}_2$  dropwise to the  $\text{NH}_4\text{OH}$  solution at a rate of approximately 2.5 mL  $\text{min}^{-1}$  using a graduated buret while we kept the latter solution vigorously stirred at a constant temperature of  $45 \pm 3$  °C. Lu and colleagues (2004) have proposed that the precipitation reaction:



occurred during the addition of  $\text{MgCl}_2$  to  $\text{NH}_4\text{OH}$ . After brucite precipitated, we set the sealed reaction vessel aside to cool at room temperature for 3 days. We thoroughly washed the soluble  $\text{NH}_4\text{Cl}$  byproduct from the precipitate with Milli-Q water. We then dried the precipitate on a Corning PC-420D hot plate at 135 °C for 1 h.

#### 2.1.1. Hydrothermal treatment

Both Henrist and coworkers (2003) and Lu and coworkers (2004) observed that the crystallinity and morphology of synthetic brucite improved when it was sealed with water in a reaction vessel heated above 100 °C over an extended period of time. We carried out a hydrothermal

aging treatment on our synthetic brucite by sealing an aqueous suspension of the synthetic brucite in Milli-Q water within a PTFE-lined stainless steel reaction vessel (Col-Int-Tech). We heated the precipitate in a furnace at 150 °C for 3 days, and after cooling the brucite–water solution to room temperature, we dried the powder at 135 °C with a hotplate. We then stored the hydrothermally-treated brucite powder in a glass vial under an Ar gas atmosphere at room temperature.

SEM imaging (JEOL 8500F) revealed that the untreated brucite has a crystal habit characterized by rosettes of rough, circular, and oblong platelets (Fig. 1a), whereas the hydrothermally-treated brucite is distinguished by clusters of lamellar, hexagonal platelets (Fig. 1b). Additionally, the powder XRD (Bruker D2 Phaser) pattern of the hydrothermally-treated brucite demonstrates higher intensity peaks in the case of reflection (001) and reduced intensity for the (100), (101) and (111) reflections (Fig. 2). This pattern is consistent with powder XRD patterns collected

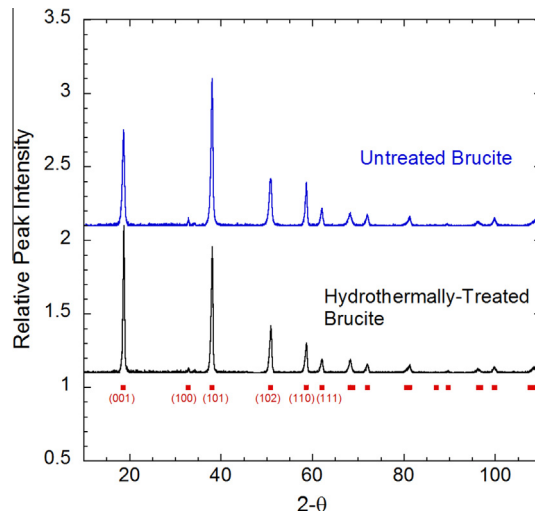


Fig. 2. Synthetic brucite powder XRD patterns, both untreated (blue) and hydrothermally treated (black). (*hkl*) reflections are indexed by the red squares. (For interpretation of the references to color in this figure legend, the reader is referred to the web version of this article.)

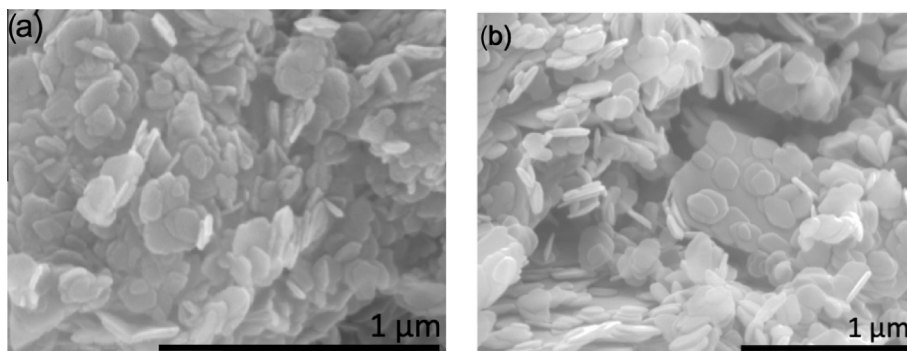


Fig. 1. SEM image of synthetic brucite (a) before hydrothermal treatment where oblong platelets are clustered in rosettes and (b) after hydrothermal treatment where platelets are hexagonal and in lamellar clusters (scale = 1  $\mu\text{m}$ ).

under ambient conditions that have been archived at the International Centre for Diffraction Data (<http://icdd.com>). Our SEM and powder XRD observations may be interpreted as evidence that the hydrothermal treatment process enhanced the crystallinity in the basal direction by reducing terraces and kink sites and improving hexagonal morphology.

## 2.2. Brucite specific surface area

We characterized the surface area of the synthetic brucite powder with the multi-point BET N<sub>2</sub> adsorption method (Micromeritics, Norcross, GA, USA) to obtain a specific surface area of  $17.6 \pm 0.1 \text{ m}^2 \text{ g}^{-1}$ . A high proportion of this measured surface area most likely represents the prominent (001) basal surface, although the distribution between the basal and lateral (edge) surfaces cannot be determined with the classical N<sub>2</sub> gas adsorption method. This distinction is important because previous adsorption studies involving mineral surfaces similar to brucite, such as gibbsite, goethite, illite, and kaolinite, conclude that only the lateral surfaces are active in the protonation and deprotonation reactions that lead to surface adsorption (Prélot et al., 2003; Sayed-Hassan et al., 2006; Liu et al., 2013). If the lateral surfaces primarily adsorb aspartate, it is necessary to determine the surface area specific to these edge surfaces.

We assayed the edge-specific surface area (ESA) with low-pressure Ar gas adsorption at the Laboratoire Interdisciplinaire des Environnements Continentaux (Vandœuvre les Nancy, France). Consistent basal- and edge-specific surface areas were previously obtained with this technique for several lamellar minerals including talc, kaolinite, illite, lamellar silica, saponite, and smectite clays (Eypert-Blaison et al., 2002; Michot and Villiéras, 2002; Villiéras et al., 2002; Tournassat et al., 2003; Sayed-Hassan et al., 2005, 2006; Perronnet et al., 2007). Other types of minerals have also been investigated with this method, including goethite, anatase, and manganese dioxide (Prélot et al., 2003; Stevanovic et al., 2010; Ali et al., 2012).

We determined a total surface area of  $19.8 \pm 0.2 \text{ m}^2 \text{ g}^{-1}$  with low-pressure Ar gas adsorption, which is comparable to the BET determined by N<sub>2</sub> gas ( $17.6 \pm 0.1 \text{ m}^2 \text{ g}^{-1}$ ). Using the methods detailed in previous studies (Villiéras et al., 1992, 1997, 2002; Tournassat et al., 2003; Sayed-Hassan et al., 2006), we have estimated that 89.5% of the surface area can be represented by basal brucite surfaces, whereas 10.5% are represented by lateral brucite surfaces (see Appendix A). We adopted a basal surface area of  $15.7 \text{ m}^2 \text{ g}^{-1}$  and a lateral surface area of  $1.9 \text{ m}^2 \text{ g}^{-1}$  by assuming that the total surface area was  $17.6 \text{ m}^2 \text{ g}^{-1}$ . We

tested these surface areas by deriving the brucite particle thickness ( $t$ ) and length ( $l$ ) with the equations:

$$l = \frac{4}{\rho \cdot S_l} \quad (4)$$

and

$$t = \frac{2}{\rho \cdot S_b} \quad (5)$$

where  $\rho$  is the density of brucite ( $2.39 \text{ g cm}^{-3}$ ) and  $S_l$  and  $S_b$  are the lateral and basal surface areas, respectively. We calculated an average brucite plate length of  $0.9 \mu\text{m}$  and thickness of  $53 \text{ nm}$ , which were consistent with the dimensions we observed with SEM ( $l = 0.1\text{--}1 \mu\text{m}$  and  $t = 30\text{--}50 \text{ nm}$ , see Fig. 1b). We therefore consider  $1.9 \text{ m}^2 \text{ g}^{-1}$  to accurately represent the ESA of the lateral surface of our brucite sample.

## 2.3. Batch adsorption experiments

In a single batch sample, we added between 2 and  $300 \mu\text{M}$  aspartate to  $10.0 \pm 0.5 \text{ g L}^{-1}$  brucite in a  $15 \text{ mL}$  sterile Falcon tube. The pH of each sample ( $10.2\text{--}10.3$  without added  $\text{MgCl}_2$ ) was strongly buffered by the brucite powder. We studied four ionic strengths that resulted from the dissolution of  $\text{Mg}^{2+}$  from brucite and our addition of either  $\text{MgCl}_2$  or  $\text{CaCl}_2$  to the aqueous phase. We conducted low- $\text{Mg}^{2+}$ , high- $\text{Mg}^{2+}$ , low- $\text{Ca}^{2+}$ , and high- $\text{Ca}^{2+}$  experiments, which we describe in Table 1.

We conducted preliminary adsorption experiments over multiple periods of time and determined that aspartate adsorption on brucite reaches a steady state within 16 h. In this study, we placed the batch samples on a test tube rotator at  $40 \text{ rpm}$  ( $25 \pm 1 \text{ }^\circ\text{C}$ , 1 bar) for 22 h to ensure that the brucite–aspartate suspensions had reached a steady state. We then measured the pH of the brucite–aspartate suspensions with a combination glass electrode (Thermo-Electron Orion 8103BNUWP) that we calibrated prior to the experiment with NIST-standardized buffers that referred to pH values of 4, 7, and 10 (Fischer Scientific). As we obtained pH measurements, we flushed each sample with Ar gas to avoid contamination by  $\text{CO}_2$ . We centrifuged the samples for 10 min with a relative centrifugal force of  $1073g$ . In each sample, we then separated the liquid supernatant from the solid brucite.

We analyzed the concentration of the aspartate,  $\text{Mg}^{2+}$  and  $\text{Ca}^{2+}$  in the supernatant with ion chromatography (IC). We used a Dionex ICS-5000 DP dual pump system equipped with an AminoPac10 column, IonPac CS12A column, and Chromeleon 6.8 software (Dionex Corporation,

Table 1

Description of the low- $\text{Mg}^{2+}$ , high- $\text{Mg}^{2+}$ , low- $\text{Ca}^{2+}$ , and high- $\text{Ca}^{2+}$  experiments. Dissolved  $\text{Mg}^{2+}$  concentrations from brucite are present in each experiment in addition to added  $\text{MgCl}_2$  and  $\text{CaCl}_2$ . All concentrations are expressed in mol/L.

Experiment	Dissolved $\text{Mg}^{2+}$	Added $\text{MgCl}_2$	Added $\text{CaCl}_2$	Ionic Strength
Low- $\text{Mg}^{2+}$	$0.7 \times 10^{-3}$	N/A	N/A	$2.1 \times 10^{-3}$
High- $\text{Mg}^{2+}$	$0.6 \times 10^{-3}$	$5.2 \times 10^{-3}$	N/A	$17.4 \times 10^{-3}$
Low- $\text{Ca}^{2+}$	$0.9 \times 10^{-3}$	N/A	$1.0 \times 10^{-3}$	$5.8 \times 10^{-3}$
High- $\text{Ca}^{2+}$	$1.0 \times 10^{-3}$	N/A	$4.0 \times 10^{-3}$	$15.2 \times 10^{-3}$

Sunnyvale, CA, USA). We analyzed the samples in triplicate and determined the mean concentration of aspartate remaining in the liquid supernatant within  $\pm 1$  standard error ( $\sigma$ ). It was necessary to analyze the aspartate samples in triplicate because we initially determined that low amounts of aspartate adsorbed onto the brucite surface ( $<10\%$ ), and collecting data in triplicate better constrained accurate aspartate adsorption values. It was not necessary for us to analyze  $\text{Ca}^{2+}$  adsorption data in triplicate because we initially observed that  $\text{Ca}^{2+}$  adsorbed onto brucite in large amounts ( $>10\%$ ), and we calculated that  $\pm 1$  standard deviation ( $\sigma$ ) was equal to about 8% of the adsorption values. From the analytical concentrations we determined the surface adsorption, ( $\Gamma_{\text{ads}}$ ,  $\mu\text{mol m}^{-2}$ ) of aspartate or  $\text{Ca}^{2+}$  on brucite, according to:

$$\Gamma_{\text{ads}} = \frac{[X]_0 - [X]_{\text{eq}}}{C_s A_s} \quad (6)$$

in which  $[X]_0$  is the initial concentration of aspartate or  $\text{Ca}^{2+}$ ,  $[X]_{\text{eq}}$  is the concentration of aspartate or  $\text{Ca}^{2+}$  remaining in the liquid supernatant,  $C_s$  is the solid concentration, and  $A_s$  is the edge-specific surface area of brucite. We report  $\Gamma_{\text{ads}}$  as an isotherm as a function of  $[X]_{\text{eq}}$ .

#### 2.4. Surface complexation modeling approach

We modeled the data from our batch adsorption experiments with the extended triple-layer model or ETLM (Sverjensky and Sahai, 1996; Sahai and Sverjensky, 1997; Sverjensky, 2003, 2005; Sverjensky and Fukushima, 2006). Unlike other solid–water interface models, the ETLM includes the electrical work resulting from the release of water dipoles during inner-sphere adsorption. We iteratively fit the adsorption data in a manner described in previous studies (Jonsson et al., 2009; Bahri et al., 2011) and obtained reaction stoichiometries that represent our best fit to the adsorption data. When it has been possible to test such surface complexation modeling with spectroscopy and quantum chemical modeling (Parikh et al., 2011; Lee et al., 2012), there has been excellent agreement as to the nature of the adsorbed species. We carried out calculations for the ETLM with the computer code GEOSURF (Sahai and Sverjensky, 1998). We estimated a  $\text{pH}_{\text{PZC}} = 10.5$  from measurements of the pH after only aspartate or water had been added to brucite during our batch adsorption experiments. We previously calculated speciation reactions involving aqueous aspartate and found them to be consistent with those determined with potentiometric titrations (De Robertis et al., 1991; Jonsson et al., 2010). We obtained both protonation and electrolyte adsorption parameters for the brucite surface from a regression of surface titration data measured by Pokrovsky and Schott (2004). As illustrated by Fig. 3, we fit these data with the ETLM using parameters that were derived from a constant capacitance model ( $C = 500 \mu\text{F cm}^{-2}$ ), where  $\text{pH}_{\text{PZC}} = 11.0$ , site density ( $N_s$ ) = 10 sites  $\text{nm}^{-2}$ , and BET surface area ( $A_s$ ) =  $9.2 \text{ m}^2 \text{ g}^{-1}$  were reported for the titration study at  $1.0 \times 10^{-2} \text{ M NaCl}$  and  $1.0 \text{ M NaCl}$ . We recalculated the protonation and electrolyte adsorption parameters for our estimated  $\text{pH}_{\text{PZC}}$ , lateral  $A_s$ , and  $N_s$  using the methods

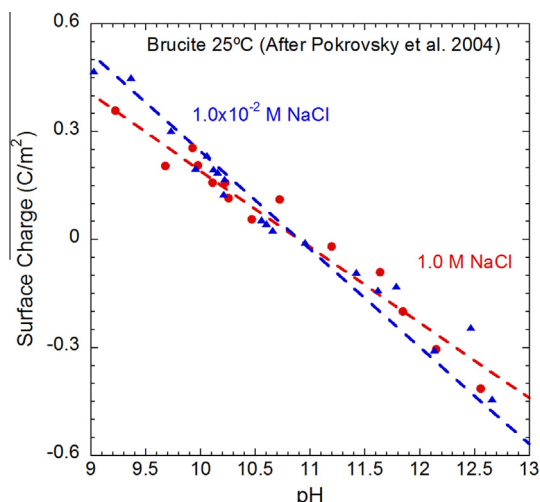


Fig. 3. Surface titration data for brucite at 25 °C determined by Pokrovsky and Schott (2004) as function of solution pH at 1.0 M NaCl (red circles) and  $1.0 \times 10^{-2} \text{ M NaCl}$  (blue triangles). Dashed curves are modeled fits to the experimental data using the ETLM and the initial parameters  $\log K_1 = 10.0$ ,  $\log K_2 = 12.0$ ,  $\log K_{\text{Na}^+} = -9.6$ ,  $\log K_{\text{Cl}^-} = -12.2$ ,  $A_s = 9.2 \text{ m}^2 \text{ g}^{-1}$ , and  $N_s = 10 \text{ sites nm}^{-2}$ . (For interpretation of the references to color in this figure legend, the reader is referred to the web version of this article.)

detailed by Sverjensky (2003, 2005). These parameters are displayed in Table 2.

Site densities can be estimated from the number of broken bonds at the surface, and these estimations are usually consistent with measurements by tritium exchange experiments (Koretsky et al., 1998). Accordingly, we calculated site densities for the lateral brucite surfaces (100), (010), (110), and (111) by examining the broken bonds of each idealized surface with the program CrystalMaker (Palmer, 2009). We estimated a minimum possible site density of 9.7 sites  $\text{nm}^{-2}$  and a maximum possible site density of 20.0 sites  $\text{nm}^{-2}$  (Table 3). However, to fit both the  $\text{Ca}^{2+}$  and aspartate adsorption data we observed for the low- $\text{Ca}^{2+}$  and high- $\text{Ca}^{2+}$  experiments, we required a site density of 38 sites  $\text{nm}^{-2}$ . This value is greater than what we estimated for the idealized surfaces, but it is consistent with site densities estimated (40.8 sites  $\text{nm}^{-2}$ ) and measured (36 sites  $\text{nm}^{-2}$ ) on periclase [ $\text{MgO}$ ], a mineral that is structurally similar to brucite and may well be covered by a thin layer of brucite in water (Anderson et al., 1965; Koretsky et al., 1998). We can also use our measurements of aspartate and  $\text{Ca}^{2+}$  adsorption to estimate site density (e.g.,  $1.0 \mu\text{mol m}^{-2} = 0.6 \text{ sites nm}^{-2}$ ). However, due to possible intermolecular forces between surface species, it may be unlikely that every active site within  $1 \text{ nm}^2$  would interact with  $\text{Ca}^{2+}$  or aspartate. It may also be possible that surface imperfections primarily caused by the dissolution of  $\text{Mg}^{2+}$  from brucite in the aqueous phase explain why it is necessary for us to adopt a higher site density. Our estimated site density of 38 sites  $\text{nm}^{-2}$  could be tested by future adsorption studies involving a variety of chemically different ions as probes of the surface.

Table 2

Aqueous aspartate properties<sup>a</sup>, characteristics of brucite<sup>b</sup>, and ETLM parameters for proton, electrolyte, and aspartate surface adsorption.

Reaction type	Reaction	log K
Aqueous aspartate equilibria	$\text{Asp}^{2-} + \text{H}^+ = \text{HAsp}^-$	10.01
	$\text{HAsp}^- + \text{H}^+ = \text{H}_2\text{Asp}$	3.88
	$\text{H}_2\text{Asp} + \text{H}^+ = \text{H}_3\text{Asp}^+$	1.92
	$\text{HAsp}^- + \text{Cl}^- + 2\text{H}^+ = \text{H}_3\text{AspCl}$	5.3
	$\text{HAsp}^- + \text{Na}^+ = \text{NaHAsp}$	-0.3
	$\text{HAsp}^- + \text{Na}^+ = \text{NaAsp}^- + \text{H}^+$	-9.6
	$\text{HAsp}^- + \text{Ca}^{2+} + \text{H}^+ = \text{CaH}_2\text{Asp}^{2+}$	-4.43
	$\text{HAsp}^- + \text{Ca}^{2+} = \text{CaHAsp}^+$	1.43
	$\text{HAsp}^- + \text{Ca}^{2+} = \text{CaAsp} + \text{H}^+$	-7.49
	Hypothetical 1.0 m standard state	
log $K_1^0$	$>\text{SOH} + \text{H}^+ \rightarrow \text{SOH}_2^+$	9.60
log $K_2^0$	$>\text{SO}^- + \text{H}^+ \rightarrow \text{SOH}$	11.40
log $K_{\text{Na}^+}^0$	$>\text{SOH} + \text{Na}^+ \rightarrow \text{SO}^-_{\text{Na}^+} + \text{H}^+$	-9.00
log $K_{\text{Cl}^-}^0$	$>\text{SOH} + \text{Cl}^- + \text{H}^+ \rightarrow \text{SOH}_2^+_{\text{Cl}^-}$	11.80
log $K_{>\text{SOH}_2^+>\text{SAsp}^-}^0$	$2>\text{SOH} + \text{H}^+ + \text{HAsp}^- \rightarrow \text{SOH}_2^+>\text{SAsp}^- + \text{H}_2\text{O}$	16.08
log $K_{>\text{SO}^-_{\text{CaHAsp}^+}}^0$	$>\text{SOH} + \text{Ca}^{2+} + \text{HAsp}^- \rightarrow \text{SO}^-_{\text{CaHAsp}^+} + \text{H}^+$	-3.73
log $K_{>\text{SOH}_2^+_{\text{Ca(OH)}_2}}^0$	$>\text{SOH} + \text{Ca}^{2+} + 2\text{H}_2\text{O} \rightarrow \text{SOH}_2^+_{\text{Ca(OH)}_2} + \text{H}^+$	-5.20
Surface equilibria <sup>c</sup>	Site-occupancy standard states	
log $K_{>\text{SOH}_2^+>\text{SAsp}^-}^0$	$2 >\text{SOH}_2^+ + \text{HAsp}^- \rightarrow \text{SOH}_2^+>\text{SAsp}^- + \text{H}_2\text{O} + \text{H}^+$	18.80
log $K_{>\text{SO}^-_{\text{CaHAsp}^+}}^0$	$>\text{SO}^- + \text{Ca}^{2+} + \text{HAsp}^- \rightarrow \text{SO}^-_{\text{CaHAsp}^+} + \text{H}^+$	-5.34
log $K_{>\text{SOH}_2^+_{\text{Ca(OH)}_2}}^0$	$>\text{SOH}_2^+ + \text{Ca}^{2+} + 2\text{H}_2\text{O} \rightarrow \text{SOH}_2^+_{\text{Ca(OH)}_2} + \text{H}^+$	-3.87

<sup>a</sup> Protonation constants and electrolyte ion pair constants from De Robertis et al. (1991), Jonsson et al. (2010).<sup>b</sup> Brucite properties are  $N_s = 38$  sites  $\text{nm}^{-2}$ ,  $A_s = 1.9$   $\text{m}^2$   $\text{g}^{-1}$ ,  $C_1 = 190$   $\mu\text{F cm}^{-2}$ ,  $C_2 = 190$   $\mu\text{F cm}^{-2}$ ,  $\text{pH}_{\text{PPZC}} = 10.5$ ,  $\Delta\text{p}K_n^0 = 2.08$ ,  $\log K_1^0 = 9.46$ ,  $\log K_2^0 = 11.54$ ,  $\log K_{\text{Na}^+}^0 = -9.14$ ,  $\log K_{\text{Cl}^-}^0 = -11.66$ .<sup>c</sup> Equilibrium constants relative to site occupancy standard states can be written relative to charged surface sites calculated using the equations:  $\log K_{>\text{SOH}_2^+>\text{SAsp}^-}^0 = \log K_{>\text{SOH}_2^+>\text{SAsp}^-}^0 + \log(N_s A_s C_s)/100$ ;  $\log K_{>\text{SO}^-_{\text{CaHAsp}^+}}^0 = \log K_{>\text{SO}^-_{\text{CaHAsp}^+}}^0 + \log(N_s A_s)/100$ ;  $\log K_{>\text{SOH}_2^+_{\text{Ca(OH)}_2}}^0 = \log K_{>\text{SOH}_2^+_{\text{Ca(OH)}_2}}^0 + \log(N_s A_s)/100$ , where  $N_s$  is site density,  $A_s$  is BET edge surface area  $\text{m}^2$   $\text{g}^{-1}$ , and  $C_s$  is solid concentration  $\text{g L}^{-1}$ .

Table 3

A summary of site densities calculated from idealized lateral brucite surfaces using the estimation procedures described by Koretsky et al. (1998) where a broken bond at a surface is considered one site per unit area. We estimated multiple site densities for every possible termination of the surfaces (100), (010), (110), and (111).

Surface	$N_s$ (Broken bonds, sites $\text{nm}^{-2}$ )
(100)	20.0
	13.4
	20.0
(010)	20.0
	13.4
	20.0
(110)	15.4
	11.6
(111)	12.9
	12.9
	9.7

With the parameters we established in Table 2, we carried out iterative fits of the adsorption data to establish the stoichiometry of surface reactions that could account for the data. We collected surface adsorption data at four ionic strengths with different dissolved ions present and a variable pH range; thus, we thoroughly tested our surface complexation model to permit the selection of a unique

set of surface reactions that successfully predict the adsorption of aspartate and  $\text{Ca}^{2+}$  onto brucite.

### 3. RESULTS AND DISCUSSION

#### 3.1. Aspartate adsorption onto brucite at low $\text{Mg}^{2+}$ concentrations

The adsorption isotherm in Fig. 4 shows the surface adsorption of aspartate on brucite as a function of the remaining aspartate concentration in the aqueous phase ( $[\text{Asp}]_{\text{eq}}$ ) when low concentrations of  $\text{Mg}^{2+}$  dissolved from the surface. We report all aspartate adsorption data in Table 4. Aspartate surface adsorption ( $\Gamma_{\text{ads}}$ ) at a pH of  $10.3 \pm 0.1$  increased steadily as a function of  $[\text{Asp}]_{\text{eq}}$ . The error in Fig. 4 is  $\pm 1 \sigma$  of each  $\Gamma_{\text{ads}}$  and  $[\text{Asp}]_{\text{eq}}$  value. Aspartate surface adsorption was between  $8.4 \times 10^{-2}$  and  $1.0 \mu\text{mol m}^{-2}$ . This range of  $\Gamma_{\text{ads}}$  corresponds to 16.4–3.6% of the initial aspartate added, where the percentage of adsorbed aspartate decreases with increasing  $\Gamma_{\text{ads}}$ . As a consequence, the reported error substantially increases with  $\Gamma_{\text{ads}}$  and  $[\text{Asp}]_{\text{eq}}$ .

As previously discussed, we assumed that only the lateral brucite surfaces were active in adsorption reactions; however, we were unable to distinguish whether there was one lateral surface that more predominantly adsorbed

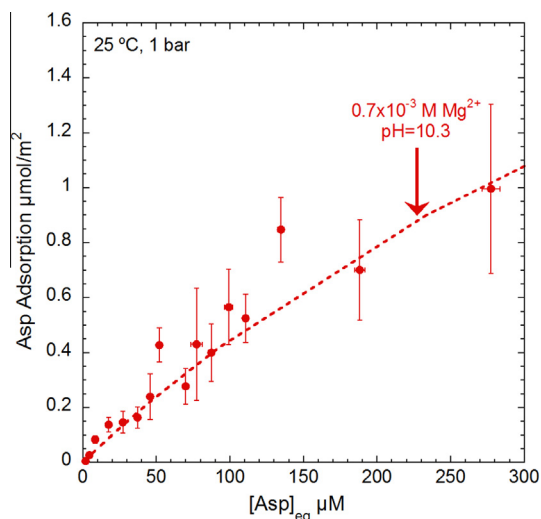


Fig. 4. Adsorption of aspartate on brucite as a function of aspartate concentration remaining in solution for the low- $\text{Mg}^{2+}$  experiments. Dashed curve represents the modeled fit to the experimental data calculated with the parameters in Table 2. Symbols represent experimental data that are the average of a triplicate run and horizontal and vertical error bars are  $\pm 1$  standard error from the average.

Table 4a

Aspartate surface adsorption data observed for the low- $\text{Mg}^{2+}$  and high- $\text{Mg}^{2+}$  batch experiments.

Batch Experiment	$[\text{Asp}]_{\text{aq}} (\mu\text{M})$	$\Gamma_{\text{ads}} (\mu\text{mol m}^{-2})$	% Ads
Low $\text{Mg}^{2+}$	4.5	0.03	10.2
	17.6	0.14	12.9
	37.3	0.16	7.8
	45.8	0.24	9.0
	70.0	0.28	7.4
	110.7	0.52	8.3
	134.7	0.85	10.8
	188.2	0.70	6.7
	1.9	0.01	3.6
	8.5	0.08	16.4
	27.3	0.15	11.6
	52.1	0.43	13.8
	77.4	0.43	9.8
	87.4	0.40	8.5
	99.2	0.57	10.3
	277.4	1.00	8.1
High $\text{Mg}^{2+}$	4.8	0.02	4.0
	9.8	0.02	4.5
	18.3	0.09	9.4
	46.1	0.20	8.1
	70.4	0.23	6.1
	95.0	0.34	6.6
	144.5	0.42	3.8
	190.4	0.52	5.0
	53.6	0.28	9.5
	36.4	0.16	7.7
	28.1	0.08	5.5
	238.4	0.63	4.3
116.0	0.19	2.5	
79.8	0.27	5.4	

Table 4b

Aspartate surface adsorption data observed for the low- $\text{Ca}^{2+}$  and high- $\text{Ca}^{2+}$  batch experiments.

Batch Experiment	$[\text{Asp}]_{\text{aq}} (\mu\text{M})$	$\Gamma_{\text{ads}} (\mu\text{mol m}^{-2})$	% Ads
Low $\text{Ca}^{2+}$	217.2	1.77	13.6
	127.2	1.20	15.3
	84.6	0.76	14.9
	61.1	0.71	18.8
	40.4	0.48	19.3
	20.3	0.25	18.8
	7.9	0.11	21.5
	4.2	0.04	17.3
	High $\text{Ca}^{2+}$	90.4	1.50
208.0		2.10	17.1
115.9		1.73	22.8
73.2		1.36	26.6
51.9		1.19	30.9
33.6		0.86	32.8
13.4		0.59	46.4
4.4		0.29	56.4
2.4		0.13	52.7

aspartate. Our crystallographic examination of the idealized lateral surfaces (100), (110), (111), and (010) revealed two distinct terminations on the three-coordinated brucite hydroxyl group: a geminal site ( $>\text{Mg}(\text{OH})_2$ ) with two bonds broken and a bridging site ( $>\text{MgOH}$ ) with a single bond broken at the surface. We could not determine whether aspartate attached at a geminal or bridging reaction site with the ETLM because our proposed surface reactions in Table 2 resulted in the same amount of electrical work at both sites. Therefore to avoid ambiguity, we display surface reactions occurring at the (100) brucite plane as an example surface only, and henceforth regard the neutral brucite surface as “ $>\text{SOH}$ ”.

We used the ETLM to carry out a series of iterative calculations to establish possible surface reactions for the aspartate. We proposed a surface reaction represented by the stoichiometry:



This reaction resulted in a close fit to the adsorption data, within analytical uncertainties, as illustrated by Fig. 4. We subsequently interpreted this surface reaction as involving a bidentate mononuclear, or “leaning” configuration with two points of attachment (one that is hydrogen-bonded and one that is inner-sphere) onto the brucite surface. A possible schematic illustration of the “leaning” surface species is shown in Fig. 5. Pokrovsky and colleagues (2005) also concluded that it was likely that biomolecules attached onto brucite through an inner-sphere attachment. Our observed range of aspartate adsorption on the brucite surface is consistent with the citrate adsorption ( $0.4 \mu\text{mol m}^{-2}$ ) measurements by Pokrovsky and coworkers (2005). Furthermore, we previously measured similar amounts of aspartate adsorption ( $1 \mu\text{mol m}^{-2}$ ) on rutile [ $\text{TiO}_2$ ], and our calculations with the ETLM also predicted an inner-sphere attachment of the aspartate molecule at the mineral–water interface (Jonsson et al., 2010).

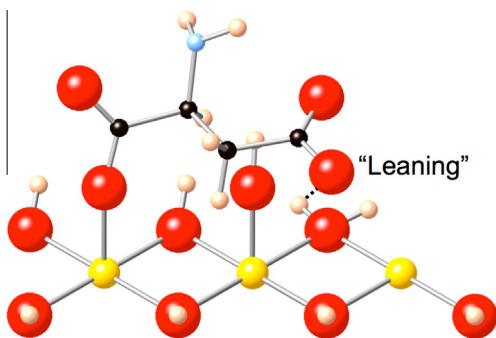


Fig. 5. Possible representation of the surface species predicted by surface complexation calculations using the parameters in Table 2 where aspartate attaches onto brucite as bidentate mononuclear, or “leaning” species. Large red spheres represent oxygen, yellow spheres are magnesium, small tan spheres are hydrogen, black spheres are carbon, and pale blue spheres are nitrogen atoms. (For interpretation of the references to color in this figure legend, the reader is referred to the web version of this article.)

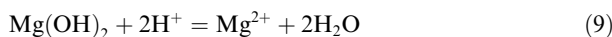
The reaction in Eq. (7) corresponds to the equilibrium constant:

$$*K_{>\text{SOH}_2^+ >\text{SAsp}^-}^0 = \frac{a_{>\text{SOH}_2^+} a_{>\text{SAsp}^-} a_{\text{H}_2\text{O}}}{a_{>\text{SOH}}^2 a_{\text{HAsp}} a_{\text{H}^+}} 10^{\frac{F\Delta\psi_{r,7}}{2.303RT}} \quad (8)$$

where the superscript “\*” indicates the reaction is expressed relative to the >SOH surface, and “0” refers to a hypothetical 1.0 molal standard state (Sverjensky, 2003). The value  $\Delta\psi_{r,7}$  represents the electrical work involved in Eq. (7). The electrical work includes a contribution from the movement of water dipoles off the brucite surface according to  $\Delta\psi_r = -n_{\text{H}_2\text{O}}(\psi_0 - \psi_\beta)$ , where  $n_{\text{H}_2\text{O}}$  are the number of water molecules on the right-hand side of the reaction. In Eq. (7),  $n_{\text{H}_2\text{O}} = 1$ , which resulted in  $\Delta\psi_{r,7} = \psi_0 - \psi_\beta$ .

### 3.2. Aspartate adsorption onto brucite at high $\text{mg}^{2+}$ concentrations

When brucite is immersed in water, the surface dissolves in aqueous solution according to:



where the equilibrium constant of Eq. (9) is:

$$\log K = \frac{a_{\text{Mg}^{2+}}}{a_{\text{H}^+}^2} \quad (10)$$

We calculated equilibrium constants of  $\log K = 17.3 \pm 0.01$  and  $\log K = 17.3 \pm 0.06$  for batch experiments in which we added only water or aqueous aspartate, respectively, to our synthetic brucite powder. These equilibrium constants are consistent with Pokrovsky and Schott’s measured value of  $\log K = 17.6 \pm 0.5$  for a ground, natural sample of brucite. We calculated the steady-state activity ratio from the activity coefficient of  $\text{Mg}^{2+}$  with GEOSURF and our measured pH values from the batch adsorption experiments. We observed that the activity ratio in Eq. (10) did not change as a function of pH (Fig. 6). Therefore, we assumed that brucite was in equilibrium with the aqueous phase during our batch adsorption

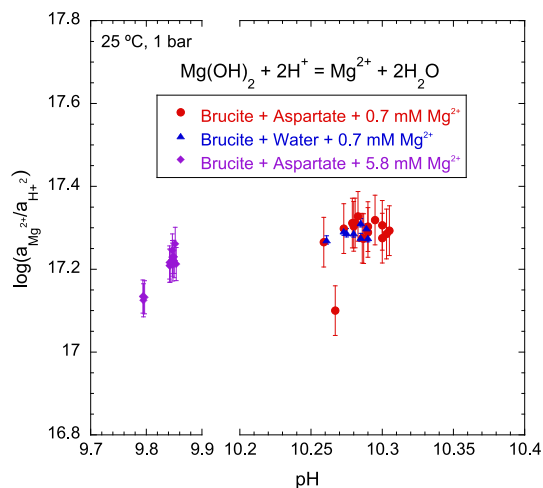


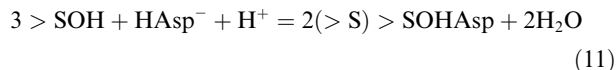
Fig. 6. Equilibrium constant for Eq. (10), or  $\log(a_{\text{Mg}^{2+}}/a_{\text{H}^+}^2)$ , as a function of solution pH for low- $\text{Mg}^{2+}$ , water, and high- $\text{Mg}^{2+}$  experiments. The vertical error bars are  $\pm 1$  standard deviation of each dataset.

experiments. If brucite was in equilibrium with the aqueous phase, we estimated that our addition of  $\text{MgCl}_2$  to an aspartate batch experiment would decrease solution pH while maintaining the equilibrium constant. We therefore calculated the activity ratio with data from the high- $\text{Mg}^{2+}$  experiment. As we predicted, pH decreased ( $\text{pH} = 9.9 \pm 0.1$ ), and the average activity ratio of  $\log K = 17.2 \pm 0.04$  was consistent within the range of uncertainty of the  $\log K$  we calculated for the low- $\text{Mg}^{2+}$  experiment.

The adsorption isotherm in Fig. 7 shows aspartate adsorption on brucite at high  $\text{Mg}^{2+}$  concentrations along with data from the low- $\text{Mg}^{2+}$  experiment. We had no indication from our IC analysis that the  $\text{MgCl}_2$  we added adsorbed onto the brucite surface. Aspartate adsorption at high  $\text{Mg}^{2+}$  concentrations was between  $1.7 \times 10^{-2}$  and  $0.6 \mu\text{mol m}^{-2}$ . In comparison with adsorption data we obtained under low  $\text{Mg}^{2+}$  concentrations,  $\Gamma_{\text{ads}}$  decreased by a factor of about 1.5.

Using the ETLM and the surface reaction proposed in Eq. (7), we predicted adsorption of aspartate for the high- $\text{Mg}^{2+}$  data at  $\text{pH} = 9.9$ . As shown in Fig. 8, there is close agreement between the curve predicted by the “leaning” aspartate species from Eq. (7) and our data at two distinct  $\text{Mg}^{2+}$  concentrations. This fit lends support to our use of the surface reaction in Eq. (7).

We also tested and dismissed dozens of other surface reactions with the ETLM. For instance, we considered the reaction stoichiometry:



which resulted in an excellent fit to the adsorption data at low  $\text{Mg}^{2+}$  concentrations. However, this reaction also predicted substantially higher amounts of aspartate adsorption (up to  $3.5 \mu\text{mol m}^{-2}$ ) at high  $\text{Mg}^{2+}$  concentrations. This strong disagreement with the experimental data led us to

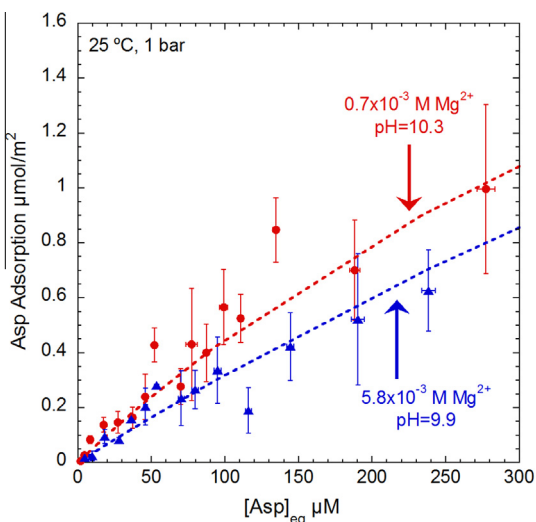


Fig. 7. Adsorption of aspartate onto brucite as a function of aspartate concentration remaining in solution for the low- $\text{Mg}^{2+}$  (red circles) and high- $\text{Mg}^{2+}$  (blue triangles) experiments. Dashed curves represent the modeled fits to the experimental data calculated with the parameters in Table 2. Symbols represent experimental data that are the average of a triplicate run and horizontal and vertical error bars are  $\pm 1$  standard error from the average. (For interpretation of the references to color in this figure legend, the reader is referred to the web version of this article.)

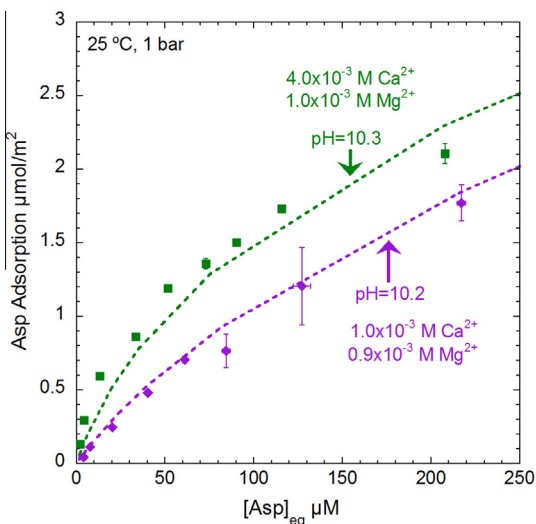


Fig. 8. Adsorption of aspartate onto brucite as a function of aspartate concentration remaining in solution for the low- $\text{Ca}^{2+}$  (purple diamonds) and high- $\text{Ca}^{2+}$  (green squares) experiments. Dashed curves represent the modeled fits to the experimental data calculated with the parameters in Table 2. Symbols represent experimental data that are the average of a triplicate run and horizontal and vertical error bars are  $\pm 1$  standard error from the average. (For interpretation of the references to color in this figure legend, the reader is referred to the web version of this article.)

dismiss this surface reaction. Through this process of elimination, we determined that only the surface reaction in Eq. (11) could predict aspartate adsorption at both  $\text{Mg}^{2+}$  concentrations.

According to the reaction in Eq. (7),  $\text{Asp}^{2-}$  attaches onto brucite. However, when the pH decreased from 10.2 in the low- $\text{Mg}^{2+}$  experiment to 9.9 in the high- $\text{Mg}^{2+}$  experiment, the abundance of the doubly-deprotonated aspartate species ( $\text{pK}_a = 10.01$ ) decreased in the aqueous phase. Therefore, the decrease in pH may have caused a decrease in aspartate adsorption.

### 3.3. Aspartate adsorption onto brucite in the presence of $\text{Ca}^{2+}$

The adsorption isotherms in Fig. 8 illustrate aspartate adsorption onto brucite in the presence of low and high  $\text{Ca}^{2+}$  concentrations. The low- $\text{Ca}^{2+}$  and high- $\text{Ca}^{2+}$  experiments were conducted at a pH of  $10.2 \pm 0.02$  and  $10.2 \pm 0.05$ , respectively. We observed that surface adsorption increased with  $\text{Ca}^{2+}$  concentration, where  $\Gamma_{\text{ads}}$  was between  $4.3 \times 10^{-2}$  and  $1.8 \mu\text{mol m}^{-2}$  for the low- $\text{Ca}^{2+}$  experiment and between 0.1 and  $2.1 \mu\text{mol m}^{-2}$  for the high- $\text{Ca}^{2+}$  experiment. The range of  $\Gamma_{\text{ads}}$  in the high- $\text{Ca}^{2+}$  experiment corresponded to between 56.4% and 17.1% aspartate adsorption, respectively.

Aspartate surface adsorption was significantly greater in the presence of  $\text{Ca}^{2+}$  compared with the low- $\text{Mg}^{2+}$  experiment (see Fig. 4). In particular, when aspartate adsorbed onto brucite at high  $\text{Ca}^{2+}$  concentrations,  $\Gamma_{\text{ads}}$  increased two-fold. In addition to this increase in aspartate adsorption, we observed that a significant amount of  $\text{Ca}^{2+}$  adsorbed onto brucite as illustrated in Fig. 9. The amount of  $\text{Ca}^{2+}$  surface adsorption averaged  $21.6 \pm 1.8 \mu\text{mol m}^{-2}$  (41.8%) for the low- $\text{Ca}^{2+}$  experiment and  $29.6 \pm 2.3 \mu\text{mol m}^{-2}$  (14.4%) for the high- $\text{Ca}^{2+}$  experiment. We report all calcium adsorption data in Table 5.

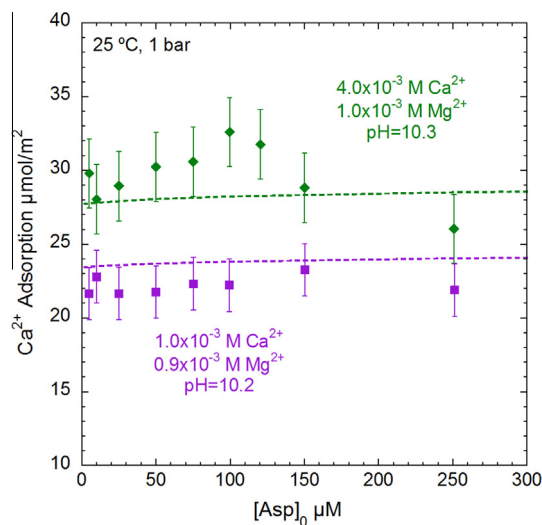
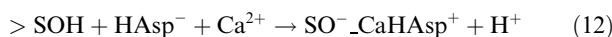


Fig. 9. Adsorption of  $\text{Ca}^{2+}$  onto brucite as a function of initial aspartate concentration determined for the low- $\text{Ca}^{2+}$  (purple squares) and high- $\text{Ca}^{2+}$  (green diamonds) experiments. Dashed curves represent the modeled fits to the experimental data calculated with the parameters in Table 2. Symbols represent experimental data and vertical error bars represent an error of 8%. (For interpretation of the references to color in this figure legend, the reader is referred to the web version of this article.)

Table 5  
Ca<sup>2+</sup> surface adsorption data observed for the low-Ca<sup>2+</sup> and high-Ca<sup>2+</sup> batch experiments.

Batch Experiment	[Ca <sup>2+</sup> ] (μM)	Γ <sub>ads</sub> (μmol m <sup>-2</sup> )	% Ads
Low Ca <sup>2+</sup>	614.1	21.88	40.7
	591.2	23.25	42.9
	605.0	22.21	41.6
	586.2	22.32	43.4
	597.4	21.75	42.3
	622.9	21.66	39.8
	597.3	22.80	42.3
	601.7	21.65	41.9
High Ca <sup>2+</sup>	3416.5	31.75	15.6
	3519.4	26.04	13.1
	3479.0	28.83	14.1
	3411.7	32.59	15.7
	3451.2	30.59	14.8
	3473.5	30.24	14.2
	3482.4	28.94	14.0
	3505.0	28.05	13.4
	3453.3	29.79	14.7

We developed a model of the surface adsorption of aspartate and Ca<sup>2+</sup> by iteratively fitting the adsorption data. We discovered that in addition to the surface reaction in Eq. (7), two surface reactions involving Ca<sup>2+</sup> were needed to fit the experimental data. The first surface reaction involved the formation of a calcium–aspartate complex:



that may attach as a monodentate outer-sphere species on brucite. Franchi and coworkers (2003) observed enhanced adsorption of nucleic acids on the clay minerals montmorillonite and kaolinite in the presence of Ca<sup>2+</sup>. The authors suggested a configuration involving calcium–nucleic acid complexes where the Ca<sup>2+</sup> ion would act as a “bridge” between the nucleic acid and the clay–water interface

(Franchi et al., 2003). We estimated a similar configuration of our predicted calcium–aspartate species at the brucite surface in Fig. 10a. We proposed that the calcium–aspartate species adsorbs in addition to the “leaning” aspartate species (Fig. 5). The equilibrium constant of the surface reaction in Eq. (12) is:

$$*K_{>\text{SO}^- \text{-Ca}(\text{HAsp})^+}^0 = \frac{a_{>\text{SO}^- \text{-}(\text{HAsp})^+} a_{\text{H}^+}}{a_{>\text{SOH}} a_{\text{HAsp}^-} a_{\text{Ca}^{2+}}} 10^{\frac{F\Delta\psi_{r,12}}{2.303RT}} \quad (13)$$

where the value  $\Delta\psi_{r,12} = -\psi_0 + \psi_\beta$ .

The second reaction we proposed required the adsorption of a hydrated calcium complex:



that can be interpreted as a monodentate outer-sphere surface species as illustrated in Fig. 10b. The equilibrium constant of the surface reaction in Eq. (14) is:

$$*K_{>\text{SOH}_2^+ \text{-Ca}(\text{OH})_2}^0 = \frac{a_{>\text{SOH}_2^+ \text{-Ca}(\text{OH})_2} a_{\text{H}^+}}{a_{>\text{SOH}} a_{\text{Ca}^{2+}} a_{\text{H}_2\text{O}}^2} 10^{\frac{F\Delta\psi_{r,14}}{2.303RT}} \quad (15)$$

where  $\Delta\psi_{r,14} = \psi_0$ .

Our proposed species differs from the prediction by Pokrovsky and coworkers (2005) that Ca<sup>2+</sup> may be attaching onto brucite as a monodentate or bidentate inner-sphere species. We tested surface reactions containing these species with the ETLM. However, they failed to adequately fit the Ca<sup>2+</sup> and aspartate adsorption data. For example, the reaction stoichiometry:



which we can alternatively express as



might result in a monodentate inner-sphere calcium species at the brucite surface. This reaction underestimated the amount of Ca<sup>2+</sup> adsorption for the high-Ca<sup>2+</sup> experiment by approximately 5.7 μmol m<sup>-2</sup>. Furthermore, the addition of this surface reaction in combination with Eqs. (7) and

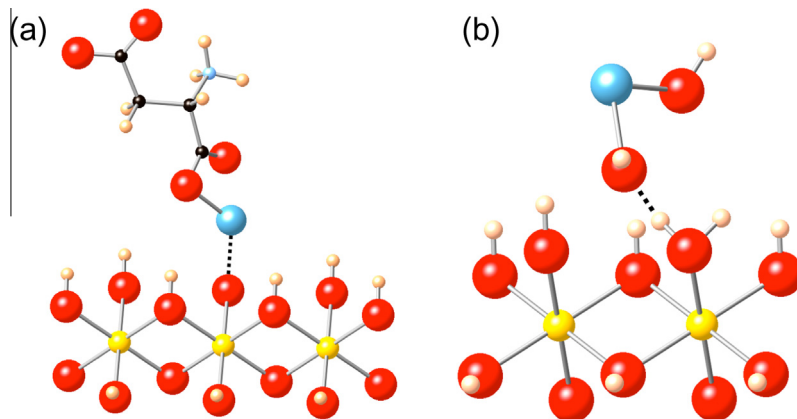


Fig. 10. Possible representation of surface species predicted by surface complexation calculations using the parameters in Table 2. (a) Attachment of a calcium–aspartate complex to the (100) surface forming a monodentate outer-sphere species through an electrostatic interaction between a surface oxygen atom and the calcium atom. (b) Attachment of a hydrated calcium molecule to the brucite surface forming a monodentate outer-sphere species. Large red spheres represent oxygen, yellow spheres are magnesium, small tan spheres are hydrogen, large light blue spheres are calcium, small pale blue spheres are nitrogen and black spheres are carbon atoms. (For interpretation of the references to color in this figure legend, the reader is referred to the web version of this article.)

(12) suppressed the amount of aspartate adsorption to less than  $0.1 \mu\text{mol m}^{-2}$  at both  $\text{Ca}^{2+}$  concentrations. We therefore could not consider Eq. (16) as a surface reaction representing  $\text{Ca}^{2+}$  adsorption onto brucite.

We combined the surface reactions in Eqs. (7), (12) and (14) to fit the aspartate adsorption data at low and high  $\text{Ca}^{2+}$  concentrations (Fig. 9). The calculated curve for the low- $\text{Ca}^{2+}$  experimental data fit within analytical uncertainty. Although in overall agreement with the isotherm shape, the curve calculated at high  $\text{Ca}^{2+}$  concentrations is a bit low compared with all of the data points except for the highest surface coverage, but is consistent with the data within  $\pm 2.5 \sigma$ , or approximately 7% uncertainty.

We predicted curves for  $\text{Ca}^{2+}$  adsorption as a function of initial aspartate concentration,  $[\text{Asp}]_0$ . As shown in Fig. 9, there are two data points from the high- $\text{Ca}^{2+}$  experiment that are elevated above the predicted curve. However, we determined that the average predicted surface adsorption of  $\text{Ca}^{2+}$  was  $28.1 \mu\text{mol m}^{-2}$ , which is well within the analytical uncertainty of the average experimental surface adsorption of  $\text{Ca}^{2+}$ ,  $29.6 \pm 2.3 \mu\text{mol m}^{-2}$ . Therefore, our prediction of  $\text{Ca}^{2+}$  surface adsorption is in acceptable agreement with the data collected at low and high  $\text{Ca}^{2+}$  concentrations. We thus regard the surface reactions proposed by Eqs. (7), (12) and (14) as sufficiently characterizing the aspartate–brucite and  $\text{Ca}^{2+}$ –brucite adsorption systems with respect to different ionic strengths, pH conditions, divalent cation concentrations and initial aspartate concentrations.

### 3.4. Prediction of brucite particle surface charge

The significant increase in aspartate adsorption with  $\text{Ca}^{2+}$  and its decrease with  $\text{MgCl}_2$  addition suggest that the particle surface charge of brucite shifted relative to the experimental conditions we investigated (Table 1). We therefore calculated the particle surface charge by predicting the  $\zeta$ -potential of the brucite surface with the ETLM as a function of  $[\text{Asp}]_0$  for each type of batch experiment. In these calculations, we assumed that the  $\zeta$ -potential was equal to the potential at the start of the diffuse layer ( $\Psi_d$ ) in the ETLM. As shown in Fig. 11, we predicted that  $\zeta$ -potential was neutral to slightly negative for the low- $\text{Mg}^{2+}$  experiment, and it decreased with increasing  $[\text{Mg}^{2+}]$ . This could be a result of decreased pH with added  $\text{MgCl}_2$ , which may directly affect the brucite surface charge. Moreover, we did not observe  $\text{Mg}^{2+}$  adsorption on brucite, although we added  $\text{MgCl}_2$  to the system. In Eq. (7), we also predicted the doubly-deprotonated aspartate molecule,  $\text{Asp}^{2-}$ , adsorbed onto brucite. A decrease in surface particle charge could create an unfavorable electrostatic environment for  $\text{Asp}^{2-}$  to adsorb onto brucite, which reflects our observation of decreased aspartate adsorption with added  $\text{MgCl}_2$ . In Fig. 11, we modeled a reversal of the  $\zeta$ -potential with  $\text{Ca}^{2+}$ . This calculation of positive particle surface charge reflects the ETLM reactions in Eqs. (12) and (14) where calcium adsorbs onto the brucite surface resulting in a net positive surface charge.

The cooperative calcium–aspartate complex,  $\text{CaHAsp}^+$ , may have enabled the aspartate molecule to adsorb in

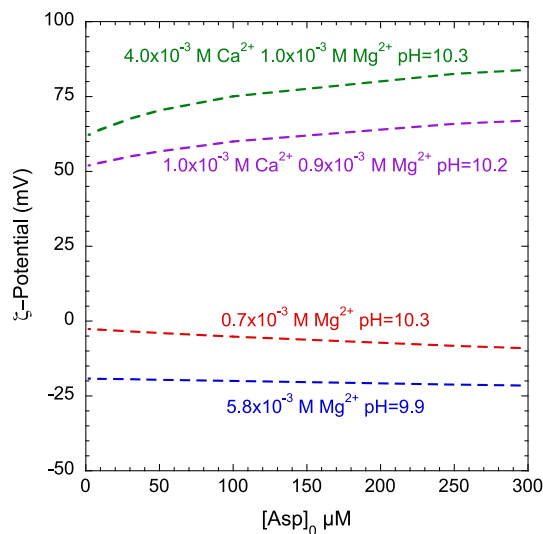


Fig. 11.  $\zeta$ -potential (mv), or particle surface charge, predicted by surface complexation modeling with the parameters in Table 2 as a function of initial aspartate concentration for the low- $\text{Mg}^{2+}$  (red), high- $\text{Mg}^{2+}$  (blue), low- $\text{Ca}^{2+}$  (purple), and high- $\text{Ca}^{2+}$  (green) experiments. (For interpretation of the references to color in this figure legend, the reader is referred to the web version of this article.)

greater amounts. We predicted the distribution of the two adsorbing aspartate species in Eqs. (7) and (12) with the ETLM at both low and high  $\text{Ca}^{2+}$  concentrations as a function of  $[\text{Asp}]_0$  in Fig. 12. At both  $\text{Ca}^{2+}$  concentrations, we observed that the calcium–aspartate outer-sphere species overwhelmingly predominates, whereas very little of the surface adsorption can be represented by the “leaning” aspartate species. This result may provide evidence that the formation of a calcium–aspartate complex enhances the adsorption of aspartate.

We predicted that a calcium–aspartate surface species forms at the brucite–water interface (Eq. 12). We predicted the distribution of aqueous aspartate species that can be represented by calcium–aspartate complexes (Fig. 13), and we determined that up to 25.8% and 6.5% of aqueous aspartate species are represented by  $\text{CaAsp}^0$  at high  $\text{Ca}^{2+}$  and low  $\text{Ca}^{2+}$  concentrations, respectively. This prediction indicates that the calcium–aspartate aqueous complex could easily form during our batch adsorption experiments. Whereas  $\text{CaAsp}^0$  predominates in aqueous solution,  $\text{CaHAsp}^+$  does not exceed 0.5% at low  $\text{Ca}^{2+}$  concentrations and 2% at high  $\text{Ca}^{2+}$  concentrations. Nevertheless, we predicted that the  $\text{CaHAsp}^+$  species predominates as a surface species, which illustrates the tendency for the mineral–water interface to adsorb organic species that may not always predominate in bulk water (Geiger, 2009; Malin et al., 2009).

It is possible that because aspartate is a polar, negatively-charged amino acid, it may readily form a cooperative complex with calcium that leads to advantageous surface adsorption on brucite. A similar amino acid, such as glutamate ( $\text{C}_5\text{H}_9\text{NO}_4$ ), may also form a complex with  $\text{Ca}^{2+}$  and follow a similar pattern of increased surface adsorption. Likewise,  $\text{Ca}^{2+}$  may not strongly bond to a positively-charged amino acid, such as lysine ( $\text{C}_6\text{H}_{14}\text{N}_2\text{O}_2$ ), and competitively adsorb with the amino acid on the brucite surface.

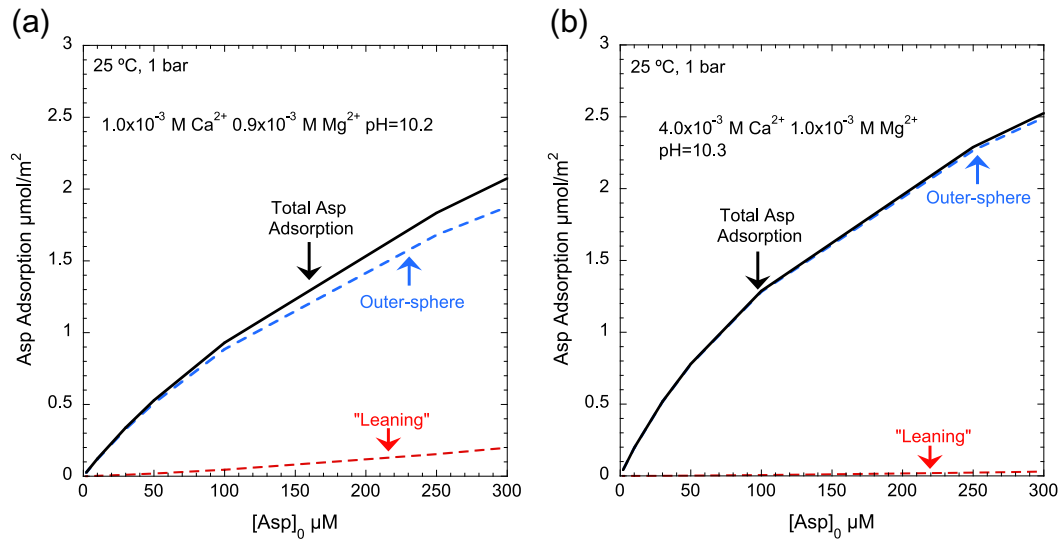


Fig. 12. The predicted surface speciation of aspartate on brucite as a function of initial aspartate concentration for the (a) low- $\text{Ca}^{2+}$  and (b) high- $\text{Ca}^{2+}$  experiments. The “leaning” and outer-sphere species refer to Fig. 5 and Fig. 10a and reaction stoichiometries in Eqs. (7) and (11), respectively. Dashed curves represent the individual species and the solid curve represents the total aspartate adsorption.

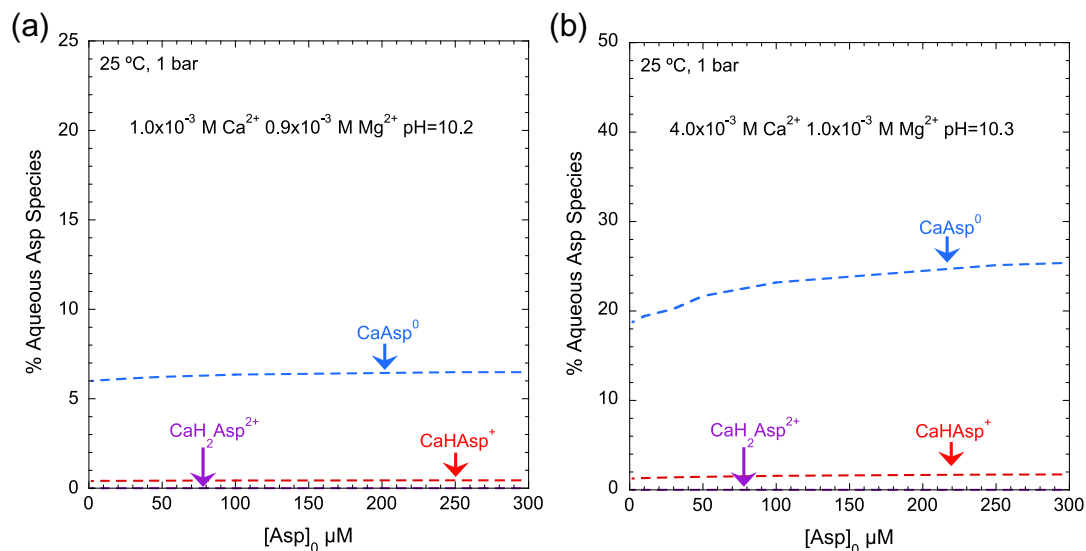


Fig. 13. The predicted distribution (%) of the aspartate aqueous species that can be represented by calcium–aspartate complexes, including  $\text{CaH}_2\text{Asp}^{2+}$ ,  $\text{CaHAsp}^+$ , and  $\text{CaAsp}^0$  as a function of initial aspartate concentration in the presence for the (a) low- $\text{Ca}^{2+}$  and (b) high- $\text{Ca}^{2+}$  experiments.

Whether  $\text{Ca}^{2+}$  may either cooperatively or competitively affect the surface adsorption of a particular biomolecule onto brucite is worth future investigation.

### 3.5. Prediction of aspartate adsorption in Lost City fluids

We propose that an ideal natural environment for aspartate to adsorb onto brucite would have elevated concentrations of  $\text{Ca}^{2+}$  and little or no  $\text{Mg}^{2+}$  present. Serpentine-hosted hydrothermal systems provide such an environment with brucite and possibly other biomolecules such as aspartate (Kelley et al., 2001; Shock and Canovas, 2010). Kelley and colleagues (2002) report that

vent fluids at the Lost City hydrothermal field have high concentrations of  $\text{Ca}^{2+}$  ( $23.3 \times 10^{-3} \text{ M}$ ) relative to a  $0 \text{ M Mg}^{2+}$  endmember composition over a pH range between 9.0 and 9.8. We invoked the surface reactions in Eqs. (7), (12) and (14) with the major ion ( $\text{Na}^+$ ,  $\text{Cl}^-$ ,  $\text{Ca}^{2+}$  and  $\text{SO}_4^{2-}$ ) concentrations reported by Kelley and coworkers (2002) to predict the surface adsorption of aspartate on brucite in Lost City vent fluids at  $25 \text{ °C}$  and  $1 \text{ bar}$ . We predicted surface adsorption at pH values of 9.8 and 10.2 (see Fig. 14). We found that surface adsorption steadily increases with a decrease in pH. For instance, we predicted that surface adsorption at a pH of 9.8 is approximately double the adsorption at a pH of

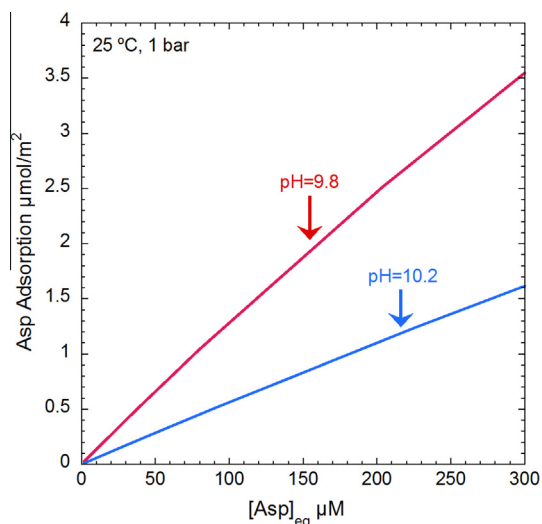


Fig. 14. Predicted aspartate surface adsorption on brucite as a function of aspartate concentration remaining in solution in the presence of Lost City-type fluids at 25 °C and 1 bar. Aspartate surface adsorption is calculated with the parameters in Table 2 in the presence of  $[\text{Na}^+] = 0.49 \text{ M}$ ,  $[\text{Cl}^-] = 0.55 \text{ M}$ ,  $[\text{Ca}^{2+}] = 23.3 \times 10^{-3} \text{ M}$ , and  $[\text{SO}_4^{2-}] = 12.9 \times 10^{-3} \text{ M}$  at a pH of 9.8 (Kelley et al., 2002) and a pH of 10.2.

10.2 at a wide range (2–300  $\mu\text{M}$ ) of aspartate concentrations. Although some of the aspartate concentrations in our predictions might exceed prebiotically-plausible concentrations of amino acids at hydrothermal vents, our model could possibly predict changes in amino acid adsorption as pH fluctuates as a consequence of an evolving hydrothermal system.

Our predictions for aspartate adsorption in the presence of the Lost City vent fluids are at ambient conditions. However, it is possible that the ETLM predictions could be extrapolated to higher temperatures in future studies if experiments are conducted under more plausible hydrothermal temperatures and pressures. It also may be that vent fluids in a Lost City-type hydrothermal field may mix with cold seawater to approximate ambient temperatures. This low-temperature environment may hold an ideal  $\text{Ca}^{2+}/\text{Mg}^{2+}$  ratio that could promote favorable aspartate adsorption onto brucite. Therefore, the results we both observed and predicted in this study appear to be highly relevant for natural serpentinite-hosted hydrothermal systems. Within this plausible prebiotic environment we have observed a cooperative surface adsorption effect between  $\text{Ca}^{2+}$  and aspartate on brucite. Our combination of batch adsorption data and surface complexation modeling contributes to a fundamental understanding of the role of the brucite–water interface in the emergence of complex biochemistry and the geochemical origin of life.

#### ACKNOWLEDGEMENTS

We would like to thank Cécile Feuillie, Namhey Lee, Alyssa K. Adcock, Timothy Strobel, Dionysis Foustoukos, Paul Goldey, John Armstrong, Adrian Villegas-Jimenez, Stephen Hodge and Steven Coley for their invaluable expertise and advice throughout this project. This research was conducted with support from the

National Science Foundation EAR-1023865 (DAS) and EAR-1023889 (RMH), Department of Energy DEFG02-96ER-14616 (DAS), NASA Astrobiology Institute, Johns Hopkins University, and the Carnegie Institution of Washington.

#### APPENDIX A. SUPPLEMENTARY DATA

Supplementary data associated with this article can be found, in the online version, at <http://dx.doi.org/10.1016/j.gca.2015.02.002>.

#### REFERENCES

- Anderson P. J., Horlock R. F. and Oliver J. F. (1965) Interaction of water with the magnesium oxide surface. *Trans. Faraday Soc.* **61**, 2754–2762.
- Ali Ahmad, M., Prélot B., Razafitianamaharavo A., Douillard J.-M., Zajac J., Dufour F., Durupthy O., Chanéac C. and Villiéras F. (2012) Influence of morphology and crystallinity on surface reactivity of nanosized anatase  $\text{TiO}_2$  studied by adsorption techniques. 1. The use of gaseous molecular probes. *J. Phys. Chem. C* **116**, 24596–24606.
- Bach W., Paulick H., Garrido C. J., Ildefonse B., Meurer W. P. and Humphris S.E. (2006) Unraveling the sequence of serpentinization reactions: petrography, mineral chemistry, and petrophysics of serpentinites from MAR 15°N (ODP Leg 209, Site 1274). *Geophys. Res. Lett.* **3**, 1–4.
- Bahri S., Jonsson C. M., Jonsson C. L., Azzolini D., Sverjensky D. A. and Hazen R. M. (2011) Adsorption and surface complexation study of L-DOPA on rutile ( $\alpha\text{-TiO}_2$ ) in NaCl solutions. *Environ. Sci. Technol.* **45**, 3959–3966.
- Baross J. A. and Hoffman S. E. (1985) Submarine hydrothermal vents and associated gradient environments as sites for the origin and evolution of life. *Orig. Life Evol. Biosph.* **15**, 327–345.
- Cleaves H. J., Chalmers J. H., Lazcano A., Miller S. L. and Bada J. L. (2008) A reassessment of prebiotic organic synthesis in neutral planetary atmospheres. *Orig. Life Evol. Biosph.* **38**, 105–115.
- Cleaves H. J., Michalkova Scott, A., Hill F. C., Leszczynski J., Sahai N. and Hazen R. M. (2012) Mineral–organic interfacial processes: potential roles in the origins of life. *Chem. Soc. Rev.* **41**, 5502–5525.
- De Robertis A., De Stefano C. and Gianguzza A. (1991) Salt effects on the protonation of L-histidine and L-aspartic acid: a complex formation model. *Thermochim. Acta* **177**, 39–57.
- Deamer D. and Pashley R. M. (1989) Amphiphilic components of the murchison carbonaceous chondrite – surface-properties and membrane formation. *Orig. Life Evol. Biosph.* **19**, 21–38.
- Dymek R. F., Brothers S. C. and Schiffrin C. M. (1988) Petrogenesis of ultramafic metamorphic rocks from the 3800 Ma Isua Supracrustal Belt, West Greenland. *J. Petrol.* **29**, 1353–1397.
- Eypert-Blaison C., Villiéras F., Michot L. J., Pelletier M., Humbert B., Ghanbaja J. and Yvon J. (2002) Surface heterogeneity of kanemite, magadiite and kenyaite: a high-resolution gas adsorption study. *Clay Miner.* **37**, 531–542.
- Franchi M., Ferris J. P. and Gallori E. (2003) Cations as mediators of the adsorption of nucleic acids on clay surfaces in prebiotic environments. *Orig. Life Evol. Biosph.* **33**, 1–16.
- Geiger F. M. (2009) Second harmonic generation, sum frequency generation, and  $\chi(3)$ : dissecting environmental interfaces with a nonlinear optical swiss army knife. *Annu. Rev. Phys. Chem.* **60**, 61–83.

- Giacomelli C. E., Avena M. J. and De Pauli C. P. (1995) Aspartic acid adsorption onto TiO<sub>2</sub> particles surface. Experimental data and model calculations. *Langmuir* **11**, 3483–3490.
- Goldschmidt V. M. (1952) Geochemical aspects of the origin of complex organic molecules on the Earth, as precursors to organic life. *New Biol.* **12**, 97–105.
- Greiner E., Kumar K., Sumit M., Giuffrè A., Zhao W., Pedersen J. and Sahai N. (2014) Adsorption of L-glutamic acid and L-aspartic acid to  $\gamma$ -Al<sub>2</sub>O<sub>3</sub>. *Geochim. Cosmochim. Acta* **133**, 142–155.
- Hazen R. M. (2005) *Genesis: The Scientific Quest for Life's Origin*. Joseph Henry Press, Washington, DC.
- Hazen R. M. (2006) Presidential address to the Mineralogical Society of America, Salt Lake City, October 18, 2005: mineral surfaces and the prebiotic selection and organization of biomolecules. *Am. Mineral.* **91**, 1715–1729.
- Hazen R. M., Filley T. and Goodfriend G. (2001) Selective adsorption of L- and D-amino acids on calcite: Implications for biochemical homochirality. *PNAS* **98**, 5487–5490.
- Hennet R., Holm N. G. and Engel M. H. (1992) Abiotic synthesis of amino-acids under hydrothermal conditions and the origin of life – a perpetual phenomenon. *Naturwissenschaften* **79**, 361–365.
- Henrist C., Mathieu J., Vogels C., Rulmont A. and Cloots R. (2003) Morphological study of magnesium hydroxide nanoparticles precipitated in dilute aqueous solution. *J. Cryst. Growth* **249**, 321–330.
- Herzberg C., Condie K. and Korenaga J. (2010) Thermal history of the Earth and its petrological expression. *Earth Planet. Sci. Lett.* **292**, 79–88.
- Holm N. G. (2012) The significance of Mg in prebiotic geochemistry. *Geobiology* **10**, 269–279.
- Holm N. G. and Andersson E. (2005) Hydrothermal simulation experiments as a tool for studies of the origin of life on earth and other terrestrial planets: a review. *Astrobiology* **5**, 444–460.
- Holm N. G., Dumont M., Ivarsson M. and Konn C. (2006) Alkaline fluid circulation in ultramafic rocks and formation of nucleotide constituents: a hypothesis. *Geochem. Trans.* **7**, 1–13.
- Hostetler P. B. (1963) The stability and surface energy of brucite in water at 25 degrees C. *Am. J. Sci.* **261**, 238–258.
- Ikhsan J., Johnson B. B., Wells J. D. and Angove M. J. (2004) Adsorption of aspartic acid on kaolinite. *J. Colloid Interface Sci.* **273**, 1–5.
- Jalbout A. F., Abrell L., Adamowicz L., Polt R., Apponi A. J. and Ziurys L. M. (2007) Sugar synthesis from a gas-phase formose reaction. *Astrobiology* **7**, 433–442.
- Jonsson C. M., Jonsson C. L., Sverjensky D. A., Cleaves H. J. and Hazen R. M. (2009) Attachment of L-glutamate to rutile ( $\alpha$ -TiO<sub>2</sub>): a potentiometric, adsorption, and surface complexation study. *Langmuir* **25**, 12127–12135.
- Jonsson C. M., Jonsson C. L., Estrada C. F., Sverjensky D. A., Cleaves, II, H. J. and Hazen R. M. (2010) Adsorption of L-aspartate to rutile ( $\alpha$ -TiO<sub>2</sub>): experimental and theoretical surface complexation studies. *Geochim. Cosmochim. Acta* **74**, 2356–2367.
- Jordan G. and Rammensee W. (1996) Dissolution rates and activation energy for dissolution of brucite (001): a new method based on the microtopography of crystal surfaces. *Geochim. Cosmochim. Acta* **60**, 5055–5062.
- Kelley D. S., Karson J., Blackman D., Fruh-Green G., Butterfield D., Lilley M., Olson E., Schrenk M., Roe K., Lebon G. and Rivizzigno P. The AT3-60 Shipboard Party (2001) An off-axis hydrothermal vent field near the Mid-Atlantic Ridge at 30 degrees N. *Nature* **412**, 145–149.
- Kelley D. S., Baross J. A. and Delaney J. R. (2002) Volcanoes, fluids, and life at mid-ocean ridge spreading centers. *Annu. Rev. Earth Planet. Sci.* **30**, 385–491.
- Kelley D. S., Karson J. A., Fruh-Green G. L., Yoerger D. R., Shank T. M., Butterfield D. A., Hayes J. M., Schrenk M. O., Olson E. J., Proskurowski G., Jakuba M., Bradley A., Larson B., Ludwig K., Glickson D., Buckman K., Bradley A. S., Brazelton W. J., Roe K., Elend M. J., Delacour A., Bernasconi S. M., Lilley M. D., Baross J. A., Summons R. T. and Sylva S. P. (2005) A serpentinite-hosted ecosystem: the Lost City hydrothermal field. *Science* **307**, 1428–1434.
- Kim H.-J., Ricardo A., Illangkoon H. I., Kim M. J., Carrigan M. A., Frye F. and Benner S. A. (2011) Synthesis of carbohydrates in mineral-guided prebiotic cycles. *J. Am. Chem. Soc.* **133**, 9457–9468.
- Koretzky C. M., Sverjensky D. A. and Sahai N. (1998) A model of surface site types on oxide and silicate minerals based on crystal chemistry; implications for site types and densities, multi-site adsorption, surface infrared spectroscopy, and dissolution kinetics. *Am. J. Sci.* **298**, 349–438.
- Kudoh Y., Kameda J. and Kogure T. (2006) Dissolution of brucite on the (001) surface at neutral pH: in situ atomic force microscopy observations. *Clays Clay Miner.* **54**, 598–604.
- Lee N., Hummer D. R., Sverjensky D. A., Rajh T., Hazen R. M., Steele A. and Cody G. D. (2012) Speciation of L-DOPA on nanorutile as a function of pH and surface coverage using surface-enhanced Raman spectroscopy (SERS). *Langmuir* **28**, 17322–17330.
- Liu X., Cheng J., Sprik M., Lu X. and Wang R. (2013) Understanding surface acidity of gibbsite with first principles molecular dynamics simulations. *Geochim. Cosmochim. Acta* **120**, 487–495.
- Lu J., Qiu L. and Qu B. (2004) Controlled growth of three morphological structures of magnesium hydroxide nanoparticles by wet precipitation method. *J. Cryst. Growth* **267**, 676–684.
- Malin J. N., Holland J. G. and Geiger F. M. (2009) Free energy relationships in the electric double layer and alkali earth speciation at the fused silica/water interface. *J. Phys. Chem. C* **113**, 17795–17802.
- McCullom T. M. and Bach W. (2009) Thermodynamic constraints on hydrogen generation during serpentinization of ultramafic rocks. *Geochim. Cosmochim. Acta* **73**, 856–875.
- Michot L. J. and Villiéras F. (2002) Assessment of surface energetic heterogeneity of synthetic Na-saponites. The role of layer charge. *Clay Miner.* **37**, 39–57.
- Noffke N., Christian D., Wacey D. and Hazen R. M. (2013) Microbially induced sedimentary structures recording an ancient ecosystem in the ca. 3.48 billion-year-old Dresser Formation, Pilbara, Western Australia. *Astrobiology* **13**, 1103–1124.
- Parikh S. J., Kubicki J. D., Jonsson C. M., Jonsson C. J., Hazen R. M., Sverjensky R. M., Sverjensky D. A. and Sparks D. L. (2011) Evaluating glutamate and aspartate binding mechanisms to rutile ( $\alpha$ -TiO<sub>2</sub>) via ATR-FTIR spectroscopy and quantum chemical calculations. *Langmuir* **27**, 1778–1787.
- Palmer D. (2009) *Crystal Maker for Mac OS X, 8.2.2*. Crystal Maker Software Limited, Oxfordshire.
- Perronnet M., Villiéras F., Jullien M., Razafitianamaharavo A., Raynal J. and Bonnin D. (2007) Towards a link between the energetic heterogeneities of the edge faces of smectites and their stability in the context of metallic corrosion. *Geochim. Cosmochim. Acta* **71**, 1463–1479.
- Pokrovsky O. S. and Schott J. (2004) Experimental study of brucite dissolution and precipitation in aqueous solutions: surface

- speciation and chemical affinity control. *Geochim. Cosmochim. Acta* **68**, 31–45.
- Pokrovsky O. S., Schott J. and Castillo A. (2005) Kinetics of brucite dissolution at 25 °C in the presence of organic and inorganic ligands and divalent metals. *Geochim. Cosmochim. Acta* **69**, 905–918.
- Ponnamperuma C. and Pering K. (1966) Possible abiogenic origin of some naturally occurring hydrocarbons. *Nature* **209**, 979–982.
- Prélot B., Villières F., Pelletier M., Gérard G., Gaboriaud F., Ehrhardt J.-J., Perrone J., Fedoroff M., Jeanjean J., Lefèvre G., Mazerolles L., Pastol J.-L., Rouchaud J.-C. and Lindecker C. (2003) Morphology and surface heterogeneities in synthetic goethites. *J. Colloid Interface Sci.* **261**, 244–254.
- Proskurowski G., Lilley M. D., Kelley D. S. and Olson E. J. (2006) Low temperature volatile production at the Lost City Hydrothermal Field, evidence from a hydrogen stable isotope geothermometer. *Chem. Geol.* **229**, 331–343.
- Roddick-Lanzilotta A. D. and McQuillan A. J. (2000) An in situ Infrared spectroscopic study of glutamic acid and of aspartic acid adsorbed on TiO<sub>2</sub>: implications for the biocompatibility of titanium. *J. Colloid Interface Sci.* **227**, 48–54.
- Sahai N. and Sverjensky D. A. (1997) Solvation and electrostatic model for specific electrolyte adsorption. *Geochim. Cosmochim. Acta* **61**, 2827–2848.
- Sahai N. and Sverjensky D. A. (1998) GEOSURF: a computer program for modeling adsorption on mineral surfaces from aqueous solution. *Comput. Geosci.* **24**, 853–873.
- Sayed-Hassan M., Villières F., Razafitianamaharavo A. and Michot L. J. (2005) Role of exchangeable cations on geometrical and energetic surface heterogeneity of kaolinites. *Langmuir* **21**, 12283–12289.
- Sayed-Hassan M., Villières F., Gaboriaud F. and Razafitianamaharavo A. (2006) AFM and low-pressure argon adsorption analysis of geometrical properties of phyllosilicates. *J. Colloid Interface Sci.* **296**, 614–623.
- Schott H. (1981) Electrokinetic studies of magnesium hydroxide. *J. Pharm. Sci.* **70**, 486–489.
- Shibuya T., Komiya T., Nakamura K., Takai K. and Maruyama S. (2010) Highly alkaline, high-temperature hydrothermal fluids in the early Archean ocean. *Precambrian Res.* **182**, 230–238.
- Shock E. L. and Canovas P. (2010) The potential for abiotic organic synthesis and biosynthesis at seafloor hydrothermal systems. *Geofluids* **10**, 161–192.
- Shock E. L. and Schulte M. D. (1998) Organic synthesis during fluid mixing in hydrothermal systems. *J. Geophys. Res.* **103**, 28513.
- Sleep N. H., Bird D. K. and Pope E. C. (2011) Serpentinite and the dawn of life. *Philos. Trans. R. Soc. Lond. B* **366**, 2857–2869.
- Stevanovic S., AliAhmad M., Razafitianamaharavo A., Villières F., Odile B., Prélot B., Zajac J., Douillard J.-M. and Chanéac C. (2010) Evidences for the relationship between surface structure and reactivity of goethite nanoparticles based on advanced molecular-probe methods. *Adsorption* **16**, 185–195.
- Sverjensky D. A. (2003) Standard states for the activities of mineral surface sites and species. *Geochim. Cosmochim. Acta* **67**, 17–28.
- Sverjensky D. A. (2005) Prediction of surface charge on oxides in salt solutions: revisions for 1:1 (M+L<sup>-</sup>) electrolytes. *Geochim. Cosmochim. Acta* **69**, 225–257.
- Sverjensky D. A. and Fukushi K. (2006) A predictive model (ETLM) for As(III) adsorption and surface speciation on oxides consistent with spectroscopic data. *Geochim. Cosmochim. Acta* **70**, 3778–3802.
- Sverjensky D. A. and Sahai N. (1996) Theoretical prediction of single-site surface-protonation equilibrium constants for oxides and silicates in water. *Geochim. Cosmochim. Acta* **60**, 3773–3797.
- Tournassat C., Neaman A., Villières F., Bosbach D. and Charlet L. (2003) Nanomorphology of montmorillonite particles: estimation of the clay edge sorption site density by low-pressure gas adsorption and AFM observations. *Am. Mineral.* **88**, 1989–1995.
- Van Kranendonk M. J. (2010) Two types of Archean continental crust: plume and plate tectonics on early Earth. *Am. J. Sci.* **310**, 1187–1209.
- Van Kranendonk M. J., Hugh Smithies R., Hickman A. H. and Champion D. C. (2007) Review: secular tectonic evolution of Archean continental crust: interplay between horizontal and vertical processes in the formation of the Pilbara Craton, Australia. *Terra Nova* **19**, 1–38.
- Villières F., Cases J. M., François M., Michot L. J. and Thomas F. (1992) Texture and surface energetic heterogeneity of solids from modeling of low pressure gas adsorption isotherms. *Langmuir* **8**, 1789–1795.
- Villières F., Michot L. J., Bardot F., Cases J. M., François M. and Rudziński W. (1997) An improved derivative isotherm summation method to study surface heterogeneity of clay minerals. *Langmuir* **13**, 1104–1117.
- Villières F., Michot L. J., Bardot F., Chamerois M., Eypert-Blaison C., François M., Gérard G. and Cases J.-M. (2002) Surface heterogeneity of minerals. *C. R. Geosci.* **334**, 597–609.

Associate editor: Tom McCollom